International Journal of Multiphase Flow 36 (2010) 608–619

Contents lists available at ScienceDirect

International Journal of Multiphase Flow

journal homepage: www.elsevier.com/locate/ijmulflow

Influence of film thickness and cross-sectional geometry on hydrophilic microchannel condensation

Chen Fang *, Milnes David, Fu-min Wang, Kenneth E. Goodson

Mechanical Engineering Department, Stanford University, Stanford, CA 94305-3032, USA

ARTICLE INFO

Article history:
Received 28 July 2009
Received in revised form 9 April 2010
Accepted 16 April 2010
Available online 27 April 2010

Keywords:
Hydrophilic microchannel
Condensation
Surface tension force
Interference fringe

ABSTRACT

Condensation in hydrophilic microchannel is strongly influenced by the channel cross-sectional geometry and the condensing surfaces hydrophobicity, which govern the evolution of the liquid film. This work makes progress on studying the relationship between channel geometry and condensation through flow regime visualizations, film-thickness measurements with optical interferometery, and temperature profile measurements with heat flux distribution construction. The hydrophilic microchannels have aspect ratios ranging from 1 to 5 and hydraulic diameters from 100 μm through 300 μm. The experimental measurement qualitatively matches the prediction of previous theoretical models accounting for the surface tension effect, which highlights the importance of surface tension force and channel geometry in the microchannel condensation. Pressure drop and mean heat flux measurements show that a larger channel is favorable for minimizing the pressure drop, while a smaller channel size and higher aspect ratio are desirable for maximizing the mean heat flux. The optimization of the channel geometry for a given application lies in the trade-off between these two factors.

1. Introduction

Understanding the physics of condensation flow and heat transfer in microchannels is important for a broad variety of engineering applications. For instance, the database for rectangular microchannel condensation heat transfer is crucial to the design of plate fin heat exchangers (Agarwal, 2006) and flat heat spreaders, in which small rectangles are the representative geometry. Prediction of the condensation heat transfer coefficient in microchannels also plays a critical role in the refrigerating system design (Hu and Chao, 2007) and the micro heat pipe technology (Chen et al., 2008a,b).

Condensation in tubes and channels at macroscales and miniscales has been extensively investigated in the past few decades, with the focus on two-phase flow patterns (Garimella, 2004; Chato, 1962; Jaster and Kosky, 1976). An observation by Mederic et al. (2005) on condensation flow patterns in tubes ranging from 10 mm to 0.56 mm in diameter showed that the tubes at macroscale and miniscale are dominated by gravity-induced asymmetrical stratified flow patterns, while in tubes smaller than 1 mm the liquid films maintain an axis-symmetrical flow pattern, highlighting the dominance of capillary forces at the smaller scales. Other experimental work (Zhang et al., 2008; Wang and Rose, 2005) showed that condensation flow patterns in microchannels deviate significantly from those at macroscales and miniscales. With the decrease in the channel size and Bond number, body forces become negligible and the surface tension force dominates the dynamics of vapor/liquid flow (Fang et al., 2008). The surface wettability and topology is of particular importance to the condensation flow in micro confined spaces, due to the strong fluid-boundary interaction (Barajas and Panton, 1992).

Since correlations developed for macroscale systems are generally not applicable at microscales, experimental work has been conducted to study microchannel condensation flow. In recent experimental work by Garimella et al. (2003) on condensation flow in round microchannels, a flow regime map was developed to predict the intermittent and annular flow patterns for various qualities. A recent study of condensation in microchannels was reported by Wu and Cheng (2005) for trapezoidal microchannels having a hydraulic diameter of 82.8 μm, in which various flow patterns, namely droplet flow and annular/injection/slug-droplet flow are observed. A similar visualization study on condensation in trapezoid silicon microchannels cooled by natural air convection was also published by Chen and Cheng (2005). In this work, stable droplet condensation was observed near the inlet, while the intermittent flow appeared downstream. Unlike flow patterns in macrochannels, annular and wavy flows were absent in the microchannel. The paper included predictions that the heat flux decreases with the channel diameter. Hu and Chao (2007) studied the water condensation in hydrophobically-treated silicon microchannels and found that the slug-bubbly flow is the dominant flow

* Corresponding author. Address: 126 Blackwelder Ct. Apt.1202, Stanford, CA, 94305, USA. Tel.: +1 650 215 3026.
E-mail address: stokesworker@gmail.com (C. Fang).

0301-9322/$ - see front matter © 2010 Elsevier Ltd. All rights reserved.
doi:10.1016/j.ijmultiphaseflow.2010.04.005

pattern in the hydrophobic silicon channel, as opposed to the film flow pattern dominating the hydrophilic channel. Zhang et al. (2008) investigated the condensation in single silicon microchannel with a high aspect ratio of 26.7, focusing on the shape, size, and the detachment frequency of the formed bubbles. Higher cooling rate resulted in a higher bubble generation frequency and smaller bubble size. The mechanism of bubble formation was also discussed.

In addition to the experimental work, various analytical and numerical models have been developed. Zhao and Liao (2002) presented an analytical model for predicting film condensation in a vertical mini-triangular channel. The condensing flow field was divided into thin film, condensate meniscus, and vapor core zones. The model showed that both pressure drop and heat transfer coefficient decrease with increasing channel size. A similar approach was also used to theoretically analyze the film condensation heat transfer in a vertical micro tube with a thin metal wire providing draining effect (Du and Zhao, 2003). The calculation showed a significant heat transfer enhancement in such channel configurations. Chen et al. (2008b) numerically studied the radius distribution of the condensate steam along triangular microchannels for annular condensation flow. The result revealed the pattern of the liquid film curvature evolution with the axial coordinate along the channel. Besides the compact model, 3D volume of fluid (VOF) method was also used by Zhang et al. to study the condensation in capillary channel (Zhang et al., 2001) and groove (Zhang and Faghri, 2001).

The previous studies showed a lack in systematic visualization and measurement of condensation in rectangular microchannel with a full range of aspect ratios and hydraulic diameters. Also, most previous studies restricted their temperature measurement to the channel inlet and outlet, and local temperature and heat transfer coefficient distribution in the microchannel is not available. The discussion of the spatial flow pattern transition mechanism is also very limited.

To address those problems, the current study explores the influence of channel geometry and film thickness on the condensational flow and heat transfer in the hydrophilic microchannel with a wide range of aspect ratios and hydraulic diameters. High speed imaging is conducted for flow pattern visualization. The temporal and spatial evolution of liquid film topology in microchannel is investigated with the aid of optical fringe inteferometry. We also discuss the measurement of temperature with 2.0 mm resolution along the channel using a thermocouple array and the heat flux reconstruction. A qualitative agreement between the experimental results and the model prediction highlights the importance of surface tension force and channel geometry in microscale condensation. The systematic measurement of pressure drop and mean heat flux for a full range of channel geometries and aspect ratios indicates that larger channels yield smaller pressure drop, whereas smaller channel size and higher aspect ratio lead to a higher mean heat flux.

2. Experimental setup and procedures

2.1. Experimental facility

Experimental apparatus is designed here to generate steam flow at designated temperature, pressure and flowrate, and achieve flow visualization and measurement. Fig. 1 shows the steam generator, steam super-heater, test section, hot air control module, and optical visualization stage. A pressure-switch-controlled electric boiler supplies saturated steam at the designated pressure and temperature. To deair the steam, the boiler is evacuated and then filled with degassed water, which is obtained by ultrasonicating heated water in a vacuum chamber for 2 h. The steam supplied by the boiler flows through a needle valve for precise flow rate regulation and an Omega PX-15 pressure transducer for channel inlet pressure measurement. The additional pressure drop due to the channel inlet/outlet manifold is estimated during the data processing and is subtracted from the pressure drop result shown in the present paper. To compensate the heat loss and avoid the condensation of steam before entering the microchannel, tubing and components between the boiler and the test section are enclosed in a super-heater whose temperature is regulated by blowing in hot air. The power of the airflow heater and the DC fan speed are subject to a PID control loop for airflow temperature stabilization. The spatial and temporal uniformity of the temperature ($\Delta T_{spatial} < 2$ °C over entire chamber, $\Delta T_{temporal} < 1.5$ °C over 1 h) in the super-heater chamber is ensured by maintaining a high and stable airflow velocity (>2 m/s). The outlet of the microchannel test section is open to the atmosphere, where the temperature and pressure are also recorded. The mass flowrate of the condensate is determined using an ACB Plus electronic scale with an accuracy of 0.5 mg. The mass flowrate is extracted from the slope of the line representing the correlation between condensate mass and time. The tubing and connections are not mechanically connected with the scale, thus exert no impact on the weight measurement.

2.2. Microchannel fabrication

Straight single microchannels with rectangular cross section are microfabricated on the silicon wafer in <1 0 0> orientation. All channels used in the present study are 60 mm in length, but differ in width and depth. Table 1 lists tested channels with their aspect ratios and hydraulic diameters. In contrast to the wet etching approach used by Chen and Cheng (2005) and Wu et al. (2007), which yields trapezoidal cross sections, the present fabrication process utilizes a plasma etching process known as Deep Reactive Ion Etching (DRIE) to etch out rectangular channels in the silicon substrate. DRIE is also used to create thru holes in the substrate that serve as inlet and outlet for the fluids. To check how perpendicular the channel sidewall is to the channel top/bottom surface, the channel width at channel top surface and bottom surface are

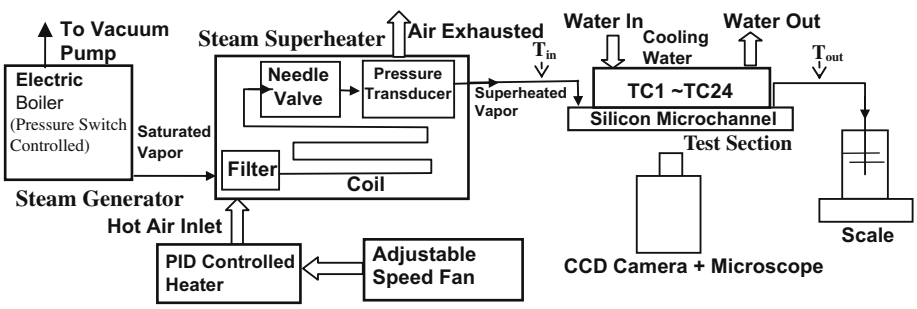

Fig. 1. Schematic diagram of experimental setup.

Table 1
Channels involved in the present paper.

Channel ID	Width (μm)	Depth (μm)	Aspect ratio	Hydraulic diameter (μm)
#1 H4	500	250	2	333.3
#2 E4	500	200	2.5	285.7
#3 A4	500	100	5	166.7
#4 E1	400	200	2	266.7
#5 A1	400	100	4	160
#6 E3	200	200	1	200
#7 A3	200	100	2	133.3
#8 B3	100	100	1	100

both measured using microscope with variable focal plane, and it is found the angle extended by the channel sidewall and top/bottom surface is approximately 87°. A Pyrex glass cover with thermal conductivity of 1.14 W/mK is anodically bonded to the wafer substrate to allow visualization of the flow and to seal the structure. Channel depth is controlled by the etching time.

2.3. Thermometry and heat transfer measurements

Fig. 2a shows the test section for flow pattern visualization and temperature distribution measurements. A cooling water chamber made of copper is used to draw the heat from the microchannel. The cooling water flows at high rate of 0.1 L/s such that the temperature rise of the water across the cooling chamber is negligible. To measure the temperature distribution on the microchannel surface, a thermocouple array is assembled by burying 24, 0.4 mm thick, type K thermocouples in a trenched copper substrate. The trench is 0.3 mm deep and 0.5 mm wide. The thermocouple junctions are equally spaced on both sides of the microchannel with an interval of 2.0 mm. The layout of thermocouple array is shown in Fig. 2b. The buried parts of the thermocouples are painted and wrapped with Teflon tape to ensure electrical insulation and to minimize inter-channel coupling. Once the test section is assembled, thermal grease is applied between the copper heat sink and the back surface of the silicon channel to reduce thermal contact resistance. The copper heat sink and silicon channel are then pressed against each other. Being slightly thicker than the trench accommodating the thermocouple, the thermocouple junctions are in close contact with the microchannel substrate. Using this arrangement the temperature distribution on the chip surface can be measured with a 2.0 mm resolution. The front surface of the microchannel chip is well insulated from the microscope stage by a 2 mm thick fiberglass layer with a thermal conductivity of 0.04 W/mK, thus the heat in the microchannel can only be drawn from its back surface and removed by the cooling water.

To reconstruct the heat flux distribution in the microchannel, the thermal contact resistance between the heat sink and the silicon chip must be determined. Since the contact resistance is strongly dependant on the contact surface condition and the contact pressure (Garimella, 2006), and may differ from case to case, the contact resistance is re-determined each time the chip in the test section is changed. To measure the contact resistance, a uniform heat flux is applied to the chip front surface by attaching a Kapton film heater, and the contact resistance can be determined following the procedure detailed in Section 4. The cooling-chamber- thermocouple-array-assembly is mounted onto the microscope stage by four bolts screwed on using a torque wrench, ensuring the same contact pressure is applied between the heat sink and chip surface for each round of testing.

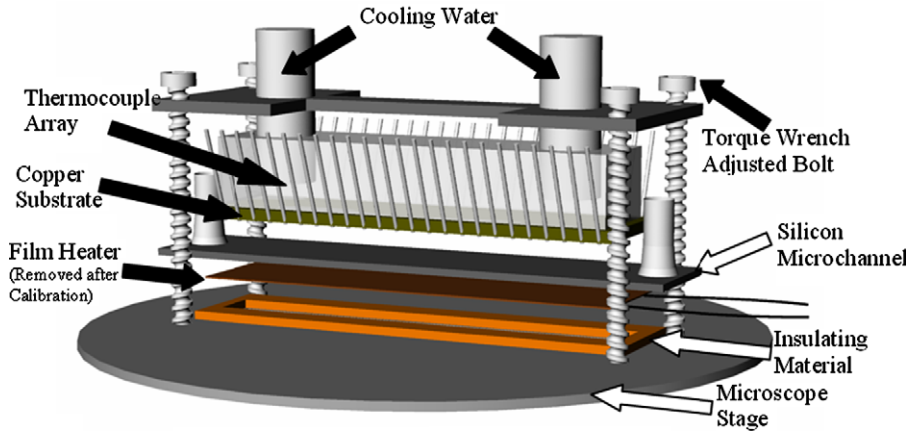

(a) Setup for local temperature measurement

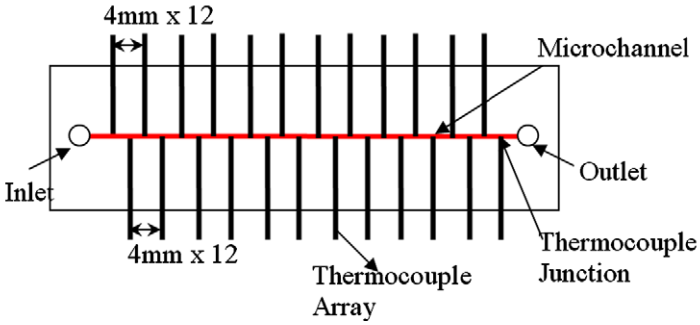

(b) Layout of thermocouple array on microchannel

Fig. 2. Setup for local temperature measurement.

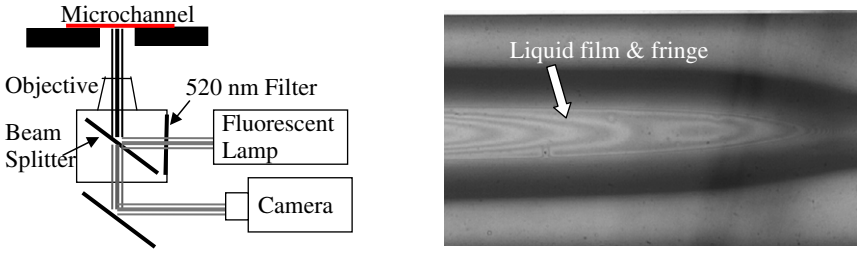

(a) light path (b) Interference fringe image indicating film topology

Fig. 3. Imaging setup configuration.

2.4. Optical visualization system

A schematic of the optical system is shown in Fig. 3a. Flow pattern visualization is carried out using a Nikon TE2000U inverted microscope, operated in reflective imaging mode with 4X and 10X objectives, and an attached Phantom v6.3 high speed CCD camera, operating at 6000 frames/s with a window size of 400 * 800 pixels. In the present study, an optical interference method is employed to obtain the topology of the thin liquid film in the microchannel. A similar approach was used by Gokhale et al. (2003) for the contact angle and droplet curvature measurement of a constrained vapor bubble.

A beam of monochromatic green light from a fluorescent lamp passes through a 520 nm filter and is partially reflected by a 50% beam splitter in the microscope to illuminate the microchannel through the microscope objective. The light reflected by the sample then passes through the beam splitter and is captured by the camera. Fringes (Fig. 3b) appear due to the interference of the light reflected by the liquid–solid and liquid–vapor interfaces. The fringes represent the contour of the liquid film thickness, with the points on two neighboring fringes differing in thickness by one wavelength, i.e. 520 nm. The 3D profile of the liquid film can thereby be reconstructed from the 2D fringe pattern. Real-time imaging of fringes indicates the transient variation of the film structure. Specifically, the film structure construction consists of three major steps: Image processing, contour digitization, and 3D interpolation. The fringes are first extracted from the raw interference image based on the pixel gradient. Then the film thickness on a grid of points is obtained from the fringe followed by a 2D interpolation yielding a smooth film thickness map. The film thickness at the channel inlet is always vanishingly small due to the superheat of the inlet vapor. Hence the reference film thickness can be determined by counting interference fringes starting from the channel inlet to the downstream.

Due to the difference in thermal conductivity, the glass is expected to be warmer than the silicon channel wall. Therefore, one expects some difference in the liquid film thickness. However, the basic pattern of liquid film evolution is expected to be similar for both surfaces, since the fundamental physical mechanism governing the liquid film evolution applies to both the glass cover and silicon microchannel wall. The current optical measurement is only intended to qualitatively reveal the pattern of liquid film evolution.

3. Flow pattern visualization and measurement

3.1. Flow patterns overview

In hydrophilic channels (Fig. 4), the upstream section of the channel wall is covered by a thin liquid film (region A). For small aspect ratio channels, a liquid layer attached to the side wall may coexist with the thin liquid film, forming an annual flow upstream. Transition from annular flow to bubbly flow occurs in

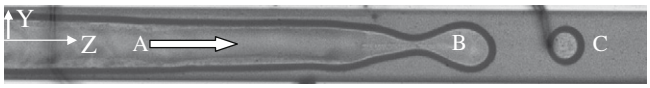

Fig. 4. Panorama view of a typical condensation flow pattern in hydrophilic microchannel #2.

the middle of the channel and features periodic growth and detachment of bubbles (region B). The detached vapor bubbles are convected downstream by the surrounding liquid while decreasing in size due to condensation (region C) until disappearing at some point. A similar flow pattern is also observed in trapezoidal silicon microchannels (Wu and Cheng, 2005; Chen and Cheng, 2005). Depending on the channel dimension and vapor flow velocity, various bubble detachment modes are observed, resulting in different bubbly flow patterns downstream to the detachment point.

3.2. Annular flow upstream (region A)

As shown in Fig. 4, thin liquid film and annular flow exists in the upstream region of the hydrophilic microchannel. Sidewall liquid layer thickness increases in the streamwise direction, accompanied by the shrinkage of the liquid film on the top and bottom channel surfaces. Fig. 5 shows the fringe patterns of liquid film at seven different locations along channel #2 at flowrate $G = 89.3\ \mathrm{kg/m^2/s}$. Superheated vapor at 150 °C is pumped into the channel, resulting in a dry region near the inlet where no stable liquid film and fringe pattern is observed (Fig. 5a). Downstream of the superheated region, the vapor is cooled to its saturation point, resulting in the condensation on the channel wall and thickening of the liquid film. This gives rise to symmetric parabola-like fringe patterns with curvature pointing downstream (Fig. 5b). The sidewall liquid layer is invisible here due to the illumination condition. Further downstream, the increase in the liquid film thickness slows and parallel fringes with a queue of rings along the center are observed, corresponding to a plateau region (Fig. 5c). Beyond the plateau region, as shown in Fig. 5d, the parabola-like fringe pattern appears with its direction reversed to the pattern seen in the thickening region upstream. Also visible in Fig. 5d is the thickening of sidewall liquid layer on both sides of the channel which is eventually terminated when the flow transitions from annular to bubbly flow. Fig. 5e illustrates the ring-shaped fringe, after which the abrupt thinning of the vapor core and the bubble detachment take place as seen in Fig. 5f.

Fig. 6 illustrates the 3D liquid film profile for four regions as constructed from the fringe patterns shown in Fig. 5 using the method introduced in Section 2.4. Due to the symmetry along the centerline only half the film structure is shown. As shown in Fig. 6a (constructed from Fig. 5b)), the parabola-like fringe indicates that the cross section of the film is thicker at the center

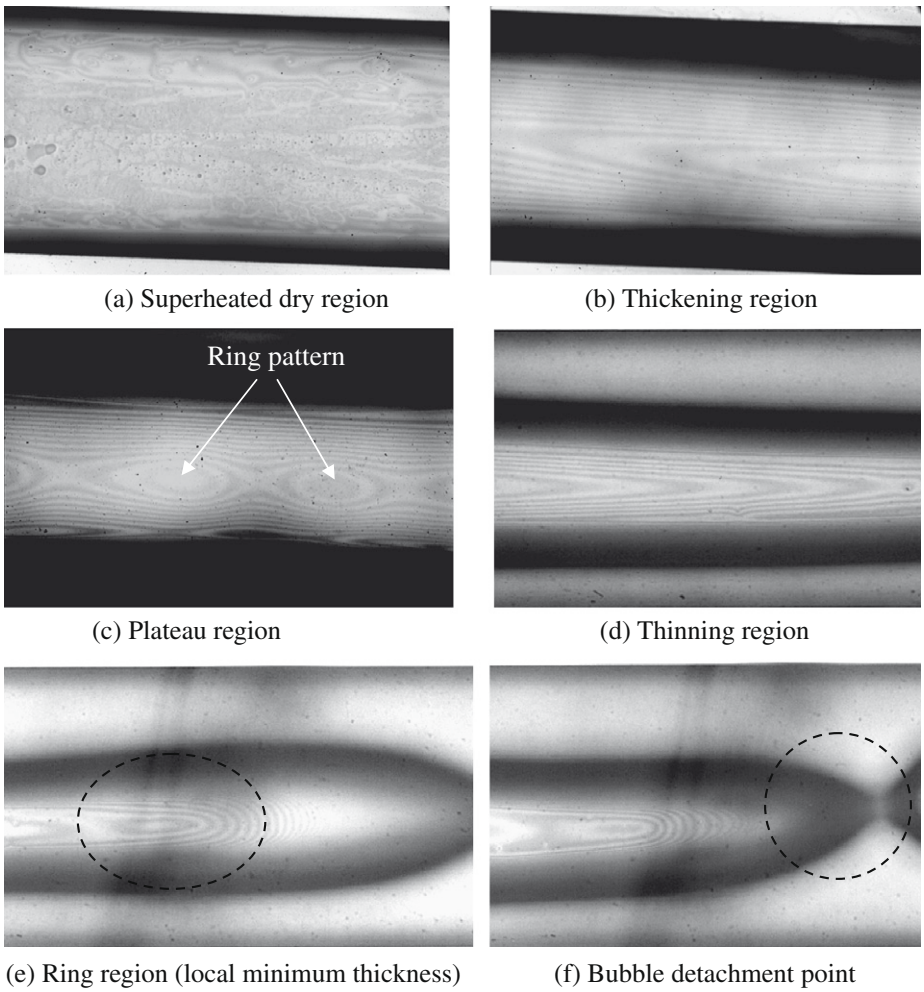

Fig. 5. Spatial evolution of fringe patterns along microchannel (channel #2, $Q = 89.3$ kg/m^2/s).

and thinner on both sides. The film merges with the sidewall liquid layer where the thickness increases abruptly and the fringe pattern becomes fuzzy. Also, starting from the zero thickness in superheated region, the film thickens in the streamwise direction. Fig. 6b (constructed from Fig. 5c) shows that the streamwise average film thickness remains fairly constant in the plateau region while the sidewall liquid layer gradually thickens. Additionally, a wave-like instability with amplitude on the order of a few microns occurs on the liquid–vapor interface. Fig. 6c (constructed from Fig. 5d) clearly shows two features of the thinning region: (1) the sidewall liquid layer thickens much faster than that in the upstream region and (2) the liquid film thickness reduces at an increasing rate, as illustrated by the reversed direction of the parabola-like fringe pattern and the decreasing spacing between neighboring fringes. In Fig. 6d (constructed from Fig. 5e), the film thickness reduces to its local minimum value, as marked by a ring pattern in Fig. 5e beyond which the liquid film suddenly thickens and periodic bubble detachment occurs. Similar to fringe patterns in the thickening region, the cross section of liquid film remains convex, i.e. thicker at center and thinner on both sides, in the plateau, thinning, and ring regions.

Fig. 7 shows the cross-section of the liquid film at various longitudinal locations for $G = 89.3$ kg/m^2/s in channel #2. The convexity of the interface is maintained from the channel inlet through the transition point. The thin film is connected with the sidewall liquid layer (not shown in the figure) at an inflection point on the curve where local minimum thickness is reached. The film thickness at the inflection point increases with z from channel inlet to the plateau region, and then decreases with z downstream. The wavy interface instability in the plateau region results in a range of interface positions with upper and lower limits shown by the error bar in Fig. 7.

Fig. 8 shows the longitudinal evolution of the liquid film thickness at channel centerline for two inlet vapor fluxes in hydrophilic channel #2. A sharp thickening near channel inlet and an abrupt thinning near transition point, with a plateau region in between, is evident. The value in the plateau region reflects a mean film thickness averaged over several periods of interface fluctuation. It is important to note that a major fraction of the channel upstream to the transition point is covered by a thin liquid film of relatively stable thickness. The comparison between two curves illustrates that lower vapor flux gives rise to a steeper thickness increase in the thickening region and slightly lower mean thickness in the plateau region. Also, lower vapor flux results in an earlier flow transition, indicated by the leftward shifting of the transition point in the plot.

It is important to note that the current optical measurement is based on channel #2 with a high aspect ratio (500 μm by 200 μm). Near the channel entrance, the water only accumulates at four corners (Fig. 9a–b). Shortly downstream, the sidewall becomes fully covered by thick liquid layer and only top/bottom wall is still covered by thin liquid film (Fig. 9c). Therefore, our discussion of thin liquid film evolution only applies to the top/bottom channel wall, while the sidewall thick liquid layer monotonously thickens

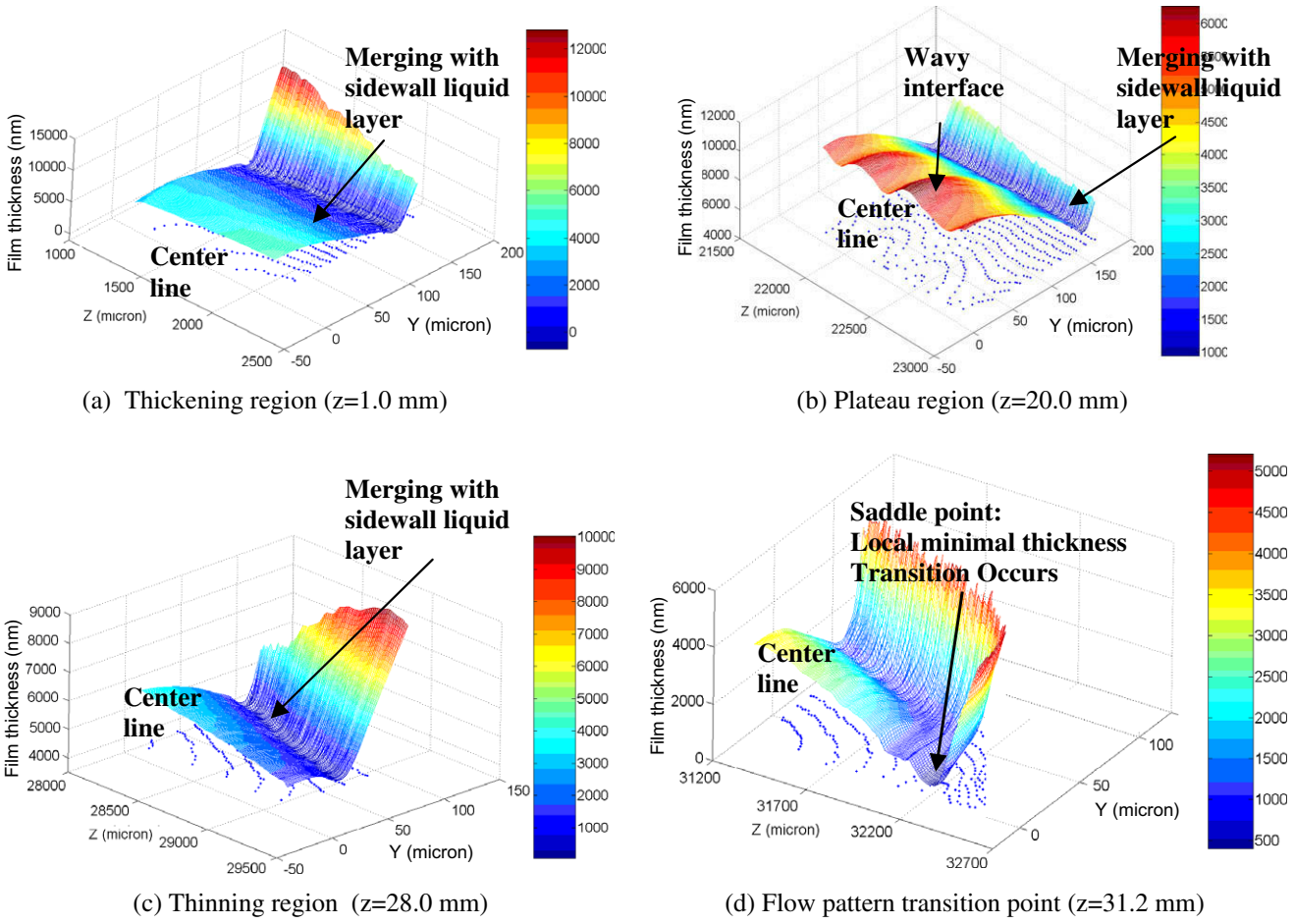

Fig. 6. 3D liquid film profile reconstructed based on fringe measurement. *Z* axis corresponds to longitudinal direction with origin located at channel inlet. *Y* axis corresponds to lateral direction, with origin located at the centerline of microchannel (see Fig. 4). Film thickness is measured w.r.t. the channel surface.

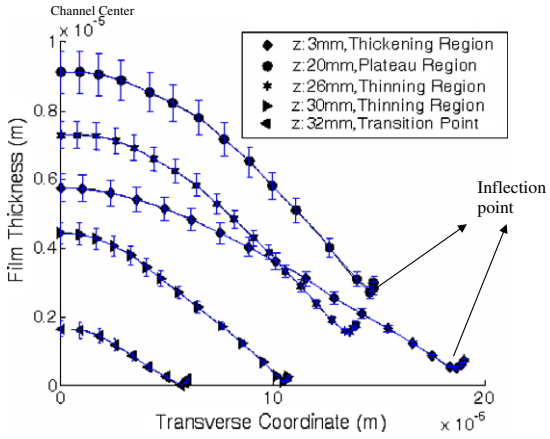

Fig. 7. Cross-sectional profile of liquid film in channel #2 ($G = 89.3$ kg/m^2/s).

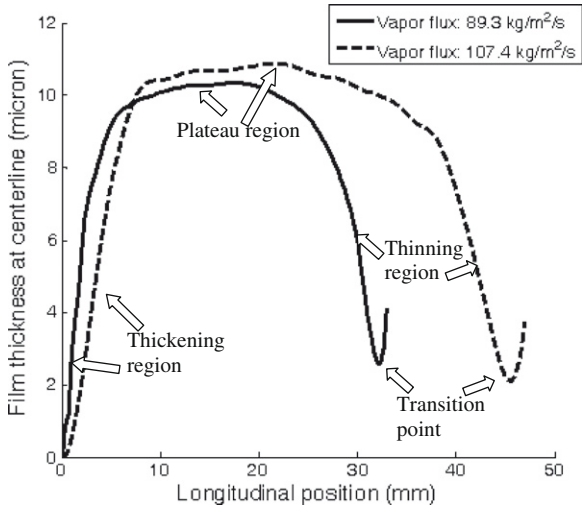

Fig. 8. Film thickness spatial evolution at centerline in channel #2.

toward to the downstream. For square channels, however, we expect the thin film evolution applies to all four channel walls.

3.3. Transition from annular to bubbly flow (region B)

As discussed in Section 3.1, transition from annular flow to bubbly flow is characterized by the periodic growth and detachment of bubbles and appears in the rectangular microchannels for various channel sizes and flow conditions. The transition mode, however, strongly depends on the inlet flowrate and channel aspect ratio. Fig. 10 shows three major modes of flow transition observed in the experiment.

In channels with moderate aspect ratio (channel #1, #2 and #4), a complete period of transition begins with the radial expansion of the tip of the vapor core to form a bubble. This bubble eventually

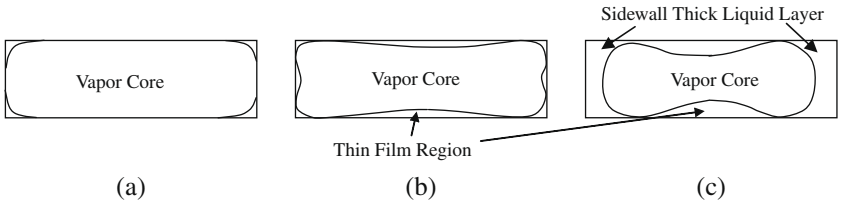

Fig. 9. Schematic of liquid–vapor interface.

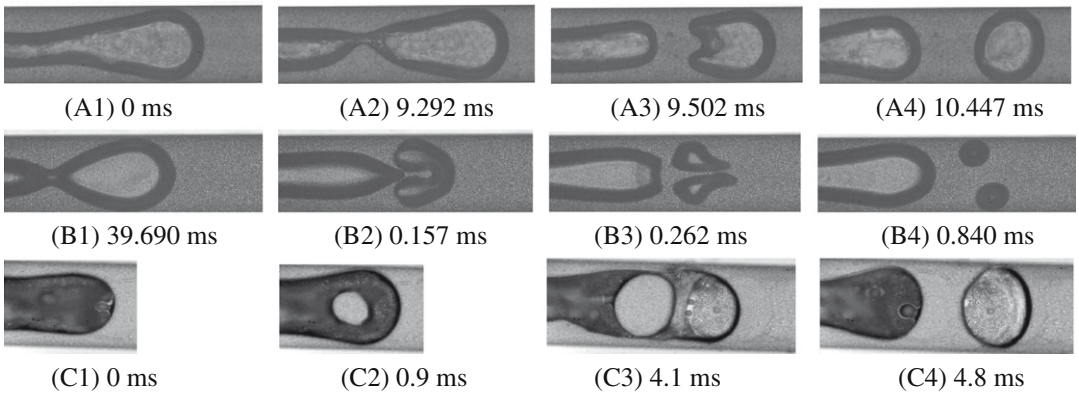

Fig. 10. Flow transition modes. A: normal detachment (channel #2, 500 * 200), B: splitting detachment (channel #2, 500 * 200), C: bifurcating detachment in high aspect ratio channel (channel #3, 500 * 100).

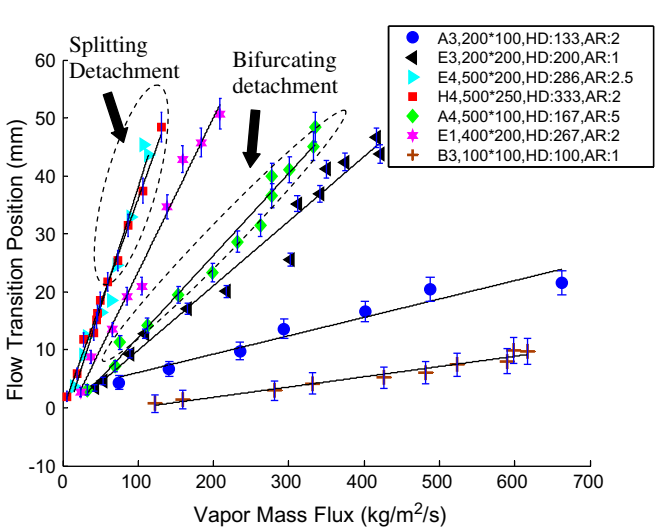

Fig. 11. Flow transition location vs. vapor mass flux for various channel geometries (HD: hydraulic diameter, AR: aspect ratio).

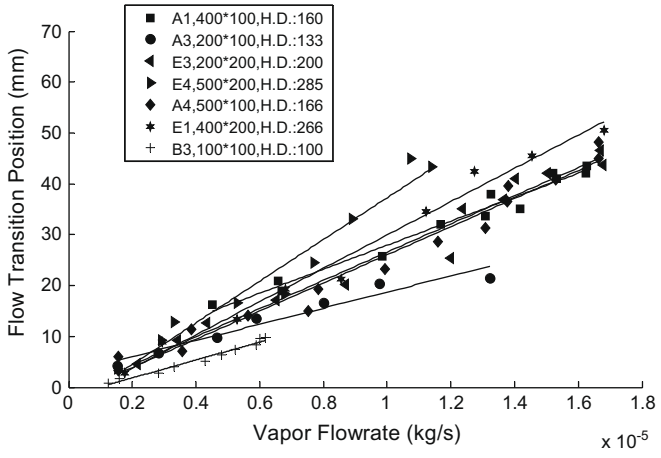

Fig. 12. Flow transition location vs. vapor mass flowrate for various channel geometries (HD: hydraulic diameter).

detaches due to continued tip expansion and thinning of the vapor core neck. If the inlet vapor flowrate is low such that the vapor core tip fails to catch up with the detached bubble, the bubble is convected downstream and the process repeats. This process is referred to as normal detachment and is shown in Fig. 10A. Similar detachment processes can also be observed in trapezoidal microchannels (Wu and Cheng, 2005; Quan et al., 2008).

Alternatively, if the inlet vapor flowrate is high enough, the abrupt buildup of pressure in the vapor core after detachment causes the tip of the vapor core to catch up and pierce into the detached bubble resulting in a splitting detachment (Fig. 10B) and the formation of a pair of small bubbles.

In channels with very high aspect ratio (channel #3), condensation may block the middle of the channel and split the single neck of the vapor core into two thin necks. The bubble eventually detaches following the simultaneous break-up of the two necks instead of the snap-off of a single neck as in the normal detachment mode, resulting in a bifurcating detachment (Fig. 10C). The bifurcating detachment was also reported by Zhang et al. (2008) which only considered high aspect ratio channels. In most other channels with low aspect ratios, the normal detachment mode dominates regardless of flowrates.

Fig. 11 shows the linear relationship between the flow transition position and the vapor mass flux at the channel inlet for various channel geometries. For the similar vapor mass flux and channel aspect ratio, channel with large hydraulic diameter yields a late flow transition. The flow conditions for splitting detachment

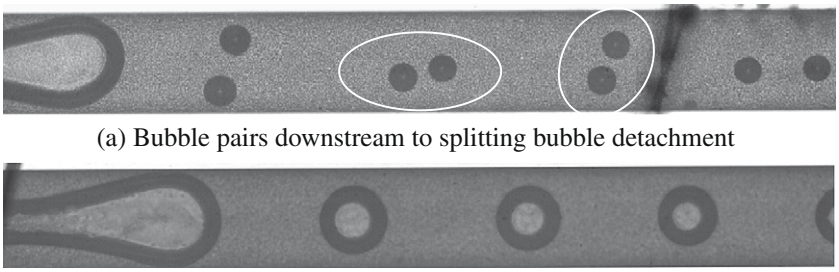

(a) Bubble pairs downstream to splitting bubble detachment

(b) Bubbly flow downstream to normal bubble detachment

Fig. 13. Bubbly flow pattern in the downstream.

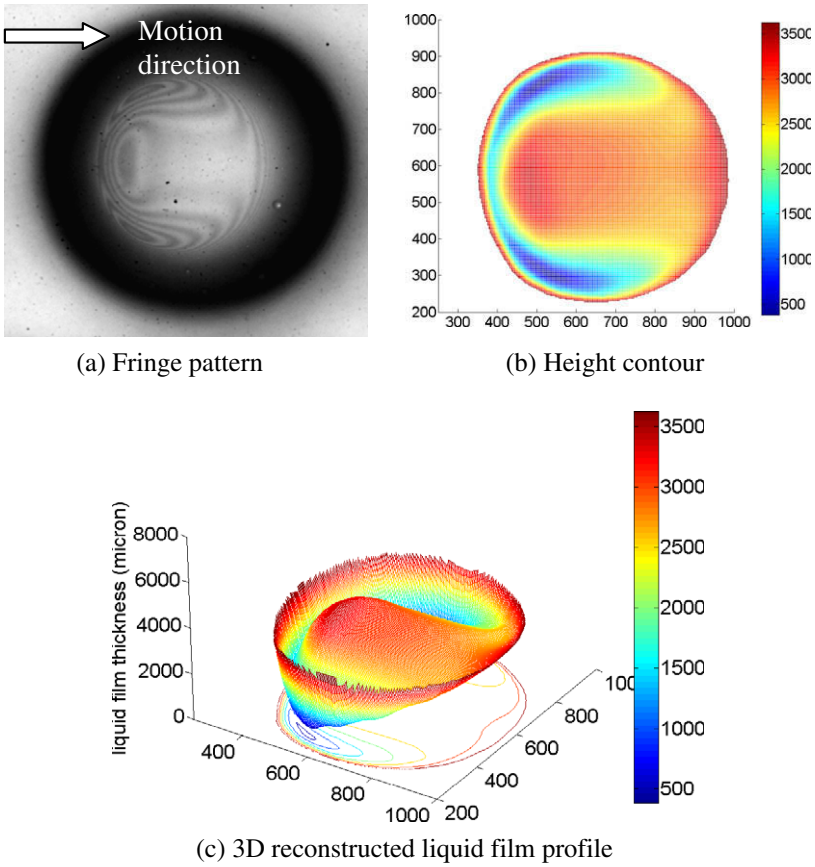

(a) Fringe pattern

(b) Height contour

(c) 3D reconstructed liquid film profile

Fig. 14. Profile reconstruction of thin film lubricating bubble motion.

and bifurcating detachment are labeled in Fig. 11 with unlabelled parts indicating normal detachment mode. Fig. 12 shows that flow transition location as a function of the vapor mass flow rate.

3.4. Bubbly flow downstream (region C)

Depending on the transition modes discussed above, bubbles downstream to the transition point vary significantly in size and spatial distribution. Fig. 13a shows bubble pairs resulting from the splitting detachment in channel #2. In contrast, a stream of circular bubbles results following normal detachment, as shown in Fig. 13b. Regardless of the size and distribution, bubbles shrink and eventually vanish due to the condensation of the vapor inside.

In hydrophilic channels, the convection of bubbles downstream is lubricated by a stable liquid film between the channel wall and bubble. The interference fringe pattern shown in Fig. 14a is used to determine the liquid film topology. Fig. 14b shows the contour of the thin film thickness, while Fig. 14c illustrates the 3D structure of the thin film topology. The dragging effect of the channel wall causes the liquid film to deform toward the bubble back-center. Note that Fig. 14c only shows the relative topology of the film interface, since the absolute thickness of the film cannot be determined solely from the interference fringes due to the lack of the zero reference point. However, the presence of the interference film indicates that the spatial variation in film thickness is comparable to the green light wavelength, i.e. on the order of a few microns.

Such pancake-shaped bubbles are only present in the high aspect ratio channel. In contrast, bubbles in the square channel are highly circular, and the liquid film between the bubble and channel wall are thicker. Considering the small thermal resistance of thin liquid films as opposed to that of thick liquid layers, high aspect ra-

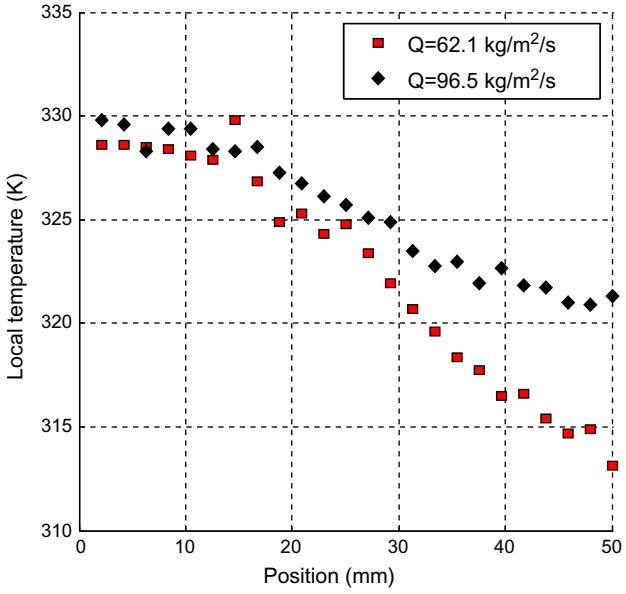

Fig. 15. Chip surface temperature distribution for two vapor fluxes in channel #2.

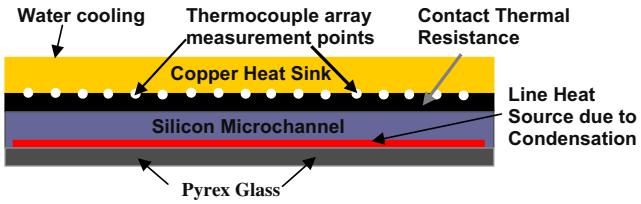

Fig. 16. Microchannel structure schematic.

tio channels are expected to be more conducive to condensation enhancement for the bubbly flow region.

4. Flow measurement

4.1. Measurement of temperature profile on channel surface

Fig. 15 shows the temperature distribution on the back surface of channel #2 for two applied flowrates. Twenty-four uniformly spaced temperature measurement points are supplied by the thermocouple array discussed in Section 2.3. Due to heat spreading and conductive thermal resistance in the silicon substrate as well as contact thermal resistance between the silicon chip and the copper heat sink with the embedded thermocouples, the temperature measured deviates substantially from the actual temperature inside the channel, which is maintained at the saturation point of water. It is found that an increase in vapor flowrate does not exert a significant impact on the temperature near the channel inlet but does delay the temperature drop in the downstream section of the channel.

4.2. Reconstruction of heat flux profile in microchannel

Reconstruction of the heat flux profile from the chip surface temperature distribution was discussed by Fang et al. (2010) with important points highlighted here. As shown in Fig. 16, the test section consists of a silicon microchannel substrate sandwiched between Pyrex glass for optical access and a copper heat sink for heat removal. The temperature field of the chip is determined by

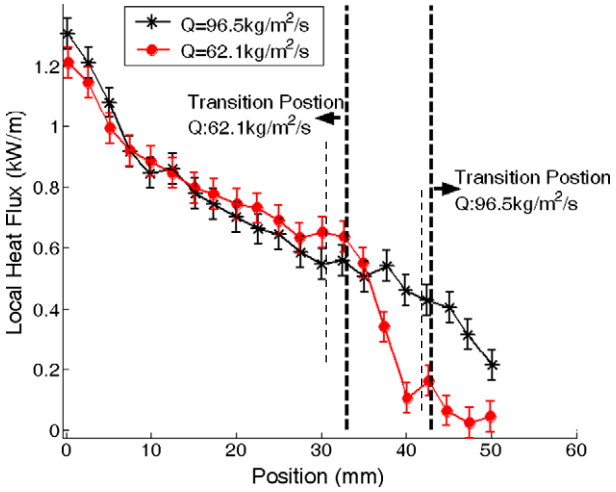

Fig. 17. Local heat flux distribution for two flowrates in channel #2.

the longitudinal heat flux distribution through the wall of a thin microchannel etched in the substrate, which can be treated as a line heat source. Taking the measured 24-point temperature on the chip surface as an input to the model, the heat flux distribution through the channel wall can be reconstructed by solving an inverse problem. Major steps include:

(1) After setting up a full CFD geometrical model replicating the real setup sketched in Fig. 16, finite volume method (FVM) is employed to solve for the temperature distribution on the chip surface by assuming the heat flux distribution of the channel, i.e. power per unit length of a line heat source. Appropriate thermal boundary condition needs to be calibrated and specified prior to the calculation.
(2) Optimize the guess of the heat flux distribution based on the criteria that the error between the calculated temperature and the measured data is minimized. In practice, the nonlinear constrained optimization algorithm simplex is used to iteratively search for the optimal combination of heat fluxes on 24 discrete points, i.e. in a 24-dimension space, based on which the continuous heat flux distribution can be obtained by piecewise spline interpolation.

As a critical thermal boundary condition, heat transfer coefficient distribution $h_c(x)$ on the water cooled side of the copper heat sink can be calibrated by applying a uniform heat flux to the Pyrex glass surface using a Kapton® film heater, and measuring the corresponding temperature distribution on the chip surface. No vapor is pumped through the channel during this process. A similar optimization approach as discussed above is employed to determine $h_c(x)$ such that the error between simulation and measurement is minimized. After the calibration step, the film heater is removed and vapor is pumped through the channel. The calibrated $h_c(x)$ can then be used for the channel heat flux reconstruction.

Fig. 17 shows the distribution of the local heat flux in channel #2 for two flowrates. Since the microchannel is treated as line heat source, a unit of W/m is used to describe the heat flux. For both flowrates, heat flux is found to initially drop sharply near the inlet, followed by a flatter decrease over a major fraction of the channel. The heat flux slumps to a very low level around the flow transition point, where mixture quality experiences a dramatic change. Transition points for the two flowrates are labeled in the plot. The heat fluxes upstream to the transition point for the two flow rates are similar, implying that the condensation heat transfer of the thin film region is not sensitive to the vapor flow rate.

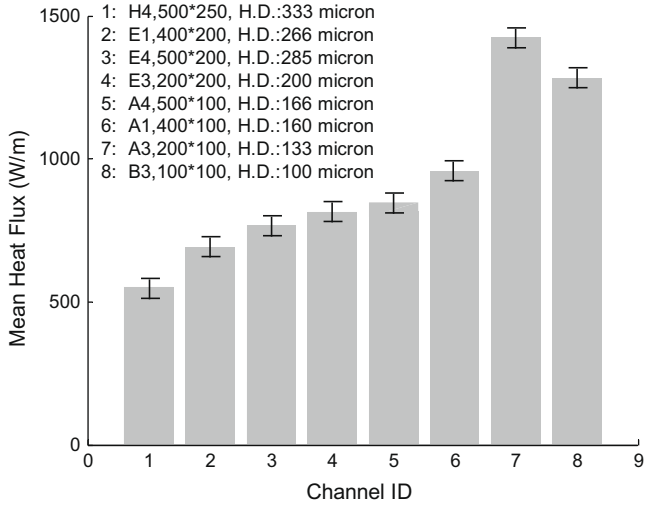

Fig. 18. Mean heat flux vs. channel for the same vapor mass flowrate (HD: hydraulic diameter).

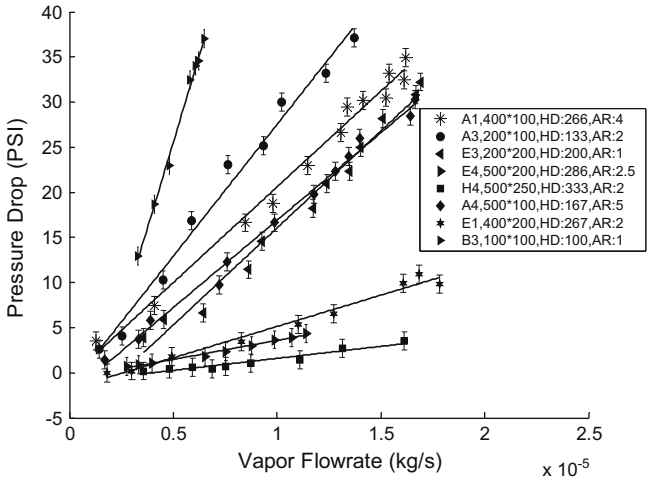

Fig. 19. Pressure drop vs. vapor flowrate for various channels (HD: hydraulic diameter, AR: aspect ratio).

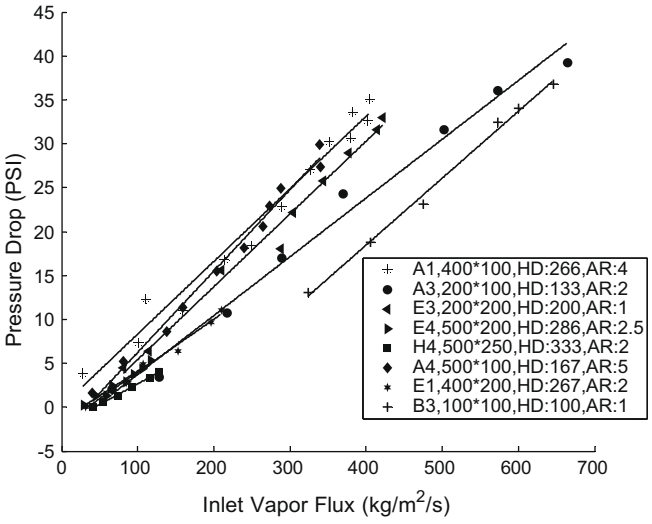

Fig. 20. Pressure drop vs. vapor flux for various channel dimensions (HD: hydraulic diameter, AR: aspect ratio).

Of great importance is the mean heat flux over the entire channel section where phase change is present. Based on the heat flux distribution measurement, mean heat flux can be obtained by dividing the integral of the local heat flux by the channel length. Fig. 18 shows the mean heat flux vs. various channels under the same vapor mass flowrate $Q = 0.5$ kg/s. If the impact of channel aspect ratio on the mean heat flux is neglected, it is found that the mean heat flux decreases almost monotonically with the channel hydraulic diameter over the full range of channels. The only exceptions are two pairs: #7 and #8, and #4 and #2, for which the trend is reversed. The reason for this anomaly is still unclear. The measurement indicates that for same mass flow rate, a smaller channel yields higher condensation heat transfer efficiency than a larger channel does.

4.3. Pressure drop characteristics

Fig. 19 shows the pressure drop for the condensing flow over the whole channel against the vapor flowrate for various channel dimensions. The correlation between the pressure drop and vapor mass flowrate is highly linear over a full range of flowrates and channel dimensions, which is similar to the characteristics of single phase flow. The plot also shows that channels with smaller hydraulic diameters yield significantly higher pressure drops, making them unfavorable due to the need for higher pumping power to deliver the vapor. Fig. 20 illustrates the pressure drop vs. vapor mass flux for various channel dimensions. Similar correlations between pressure drop and vapor flux are obtained for all channel dimensions.

5. Results and discussion

A compact model for predicting liquid film evolution during condensation in triangular microchannels was first proposed by Zhao and Liao (2002), the key idea of which includes dividing the two-phase flow field into three regions: (i) thin liquid film on the sidewall, (ii) liquid column at the corner and (iii) vapor core flow in the center. Based on a similar approach, Wang and Rose extended the channel geometry to include noncircular cross section (Wang and Rose, 2005). Both studies predicted a convex-shaped profile of the liquid film cross section in the thin film zone, with the crest located at the channel center, which qualitatively matches the present experimental measurements shown in Fig. 7. As a modification to the constant temperature boundary condition used in the previous studies, Wu et al. (2009) considered condensation film evolution in rectangular channels with a constant heat flux boundary condition. Zero film thickness at the channel inlet is also assumed, satisfying the inlet condition of the present experiment. The calculation predicts the film thickness at the channel center first increases near the inlet, and then reduces downstream, which qualitatively agrees with the results depicted in Fig. 8. As shown in Fig. 21, the condensation-induced liquid addition to the thin liquid film is balanced by the sum of the capillarity-induced liquid transfer from thin liquid film region to the sidewall thick liquid layer and the viscous-drag-induced liquid transfer to the downstream. Also, the rate of condensation-induced liquid addition to the thin liquid film is proportional to the local liquid thickness, since the local liquid film thickness determines the local thermal resistance which in turn dictates the condensation rate. Moving downstream from the channel inlet, the vapor flow initially slows down due to the loss of vapor phase caused by condensation. Hence, the viscous-drag-induced liquid transfer to the downstream decreases and the mass balance leads to the thickening of the liquid film and the decrease in the condensation-induced liquid addition. Moving further downstream, the sidewall liquid

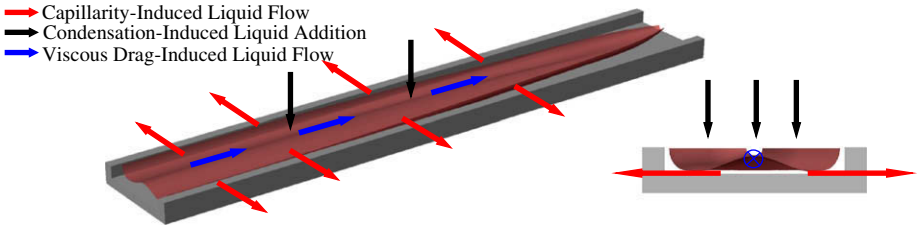

Fig. 21. Mass balance in thin liquid film.

layer thickens and the thin film region shrinks. To compensate the effect of the shrinkage of the condensation area, the film thickness has to drop to reduce the thermal resistance such that the condensation-induced liquid addition remains constant and the mass balance satisfied. The qualitative consistency between the model predication and the experimental measurement highlights the critical role surface tension, viscous force, and phase change jointly play in shaping the film profile and determining the film thickness evolution along the channel.

As opposed to the constant heat flux boundary condition assumed by Chen et al. (2008a,b) and constant temperature boundary condition used by Zhao and Liao (2002) and Wang and Rose (2005), the actual thermal boundary in our experiment is, according to the local heat flux measurement and reconstruction, neither constant heat flux nor isothermal. The present film profile measurement is also performed on a high aspect ratio channel for which theoretical data is not available in literature. Hence, further modifications to the previous microscale film condensation model is desired before quantitative comparison between model prediction and experimental measurement can be conducted and hence will be addressed in future publications.

The distribution of heat flux along the channel as seen in Fig. 17 can also be explained by considering the impact of liquid film thickness and sidewall liquid layer thickness. The condensation thermal resistance on the channel wall is primarily determined by the liquid film thickness and the effective condensation surface area. At the channel inlet, the heat flux initially decreases sharply due to the abrupt thickening of the liquid film. The heat flux curve then reduces more gradually in the middle of the channel due to the almost constant average film thickness and the gradual thickening of the sidewall liquid layer. The sharp drop in heat flux near the transition point is attributed to the sudden increase in sidewall liquid layer thickness, which dramatically reduces the effective condensation area, i.e. thin film area.

As shown in Fig. 18, a smaller channel yields higher condensation heat transfer efficiency than a larger channel. For a fixed vapor mass flow rate, a smaller channel yields a higher vapor velocity, which results in a thinner liquid film on the channel wall. The enhancement of heat transfer efficiency in a smaller channel is primarily caused by the reduction in the thermal resistance due to the reduced liquid film thickness.

6. Summary and concluding remarks

The present paper experimentally investigates the condensation flow in rectangular hydrophilic microchannels based on high speed imaging and parametric measurement. The main conclusions include:

1. In hydrophilic channels, stable liquid film and annular flow exists in the upstream region of the microchannel followed by transition to bubbly flow in the middle, a process featured by periodic growth and detachment of bubbles. Further condensation causes the bubbles to shrink and eventually disappear as they are advected downstream. Depending on channel aspect ratio and vapor inlet velocity, various bubble detachment modes including normal, bifurcating, and splitting detachment are observed, resulting in different bubbly flow patterns downstream of the detachment point. The flow pattern transition is delayed for channels with larger hydraulic diameters and for higher vapor flux rates.
2. Optical interference shows the topology of the thin liquid film present in the upstream region of high aspect ratio channels. In the transverse direction, the thickness of the film gradually decreases from the channel centerline to the sides, followed by an abrupt increase when the film merges with the sidewall liquid layer. In the streamwise direction, the film first thickens quickly until reaching a fairly constant thickness in the plateau region, which dominates a large fraction of the channel length. Wavy instability on the liquid–vapor interface with amplitude on the order of micron becomes significant in this region. Approaching the transition point from annular to bubbly flow the liquid film thickness decreases rapidly until eventually reaching a local minimum as illustrated by a ring pattern of interference fringes. Beyond this minimum the film thickness sharply increases again and a bubble detachment process takes place. The qualitative match between previous model prediction and present experimental measurements is a good indication that surface tension force plays a vital role in forming the liquid film topology.
3. Combination of 3D film profile measurement and heat flux distribution measurement indicates that heat flux initially decreases sharply due to the rapid thickening of the liquid film. The reduction in the heat flux curve is more gradual in the middle of the channel due to the stable film thickness and the gradual thickening of the sidewall liquid layer in that section. The sharp drop of heat flux near the transition point is attributed to the sudden increase in sidewall liquid layer thickness, which in turn dramatically reduces the effective condensation area, i.e. thin film area.
4. Pressure drop increases linearly with both inlet vapor mass flux and inlet vapor mass flowrate. Under the same vapor flow rate and aspect ratio, the channel with the smaller hydraulic diameter exhibits the higher pressure drop.
5. While the pressure drop reduces with increasing hydraulic diameters so does the mean heat flux. Therefore, the optimization of hydrophilic channel geometry for film condensation enhancement lies in the trade-off between these two factors. If the pumping power of the compact heat exchanger is of primary concern, a larger channel is more desirable considering its small pressure drop. In contrast, if heat exchanger size or channel length is the primary limit, a smaller channel is more favorable due to its high mean heat flux.

Acknowledgements

The authors are grateful for the support of this work by Stanford Graduate Fellowship and Honda R&D Co., Ltd. Silicon microchannels used in the present study were fabricated at the Stanford

Nanofabrication Facility (a member of the National Nanofabrication Users' Network) which is supported by the National Science Foundation under Grant ECS-9731293. The authors also would like to thank Applied Microstructures Inc. for their chip coating services.

References

Agarwal, A., 2006. Heat Transfer and Pressure Drop During Condensation of Refrigerants in Microchannels, Ph.D. Dissertation, Georgia Institute of Technology.

Barajas, A.M., Panton, R.L., 1992. The effect of contact angle on two-phase flow in capillary tubes, Int. J. Multiphase Flow 19, 337.

Chato, J.C., 1962. Laminar condensation inside horizontal and inclined tubes. ASHRAE J. 4, 52–60.

Chen, Y., Cheng, P., 2005. Condensation of steam in silicon microchannels 32. Int. Comm. Heat Mass Transfer 32, 175–183.

Chen, Y., Shi, M., Cheng, P., Peterson, G., 2008a. Condensation in microchannels. Nanoscale Microscale Thermophys. Eng. 12, 1–27.

Chen, Y., Wu, J., Shi, M., Peterson, G., 2008b. Numerical simulation for steady annular condensation flow in triangular microchannels. Int. Comm. Heat Mass Transfer 35, 805–809.

Du, X., Zhao, T., 2003. Analysis of film condensation heat transfer inside a vertical micro tube with consideration of the meniscus draining effect. Int. J. Heat Mass Transfer 46, 4669–4679.

Fang, C., Carlos, C., Wang, F., Eaton, J., Goodson, K., 2008. 3-D numerical simulation of contact angle hysteresis for microscale two phase flow. Int. J. Multiphase Flow 34, 690–705.

Fang, C., Steinbrenner, J., Wang, F., Goodson, K., 2010. Impact of wall hydrophobicity on condensation flow and heat transfer in silicon microchannels. J. Micromech. Microeng. 20, 045018.

Garimella, S., 2004. Condensation flow mechanisms in microchannels: basics for pressure drop and heat transfer models. Heat Transfer Eng. 25, 104–116.

Garimella, S.V., 2006. Advances in mesoscale thermal management technologies for microelectronics. Microelectron. J. 37, 1165–1185.

Garimella, S., Killion, J., Coleman, J., 2003. An experimentally validated model for two-phase pressure drop in the intermittent flow regime for circular microchannels. J. Fluids Eng. 125, 887–894.

Gokhale, S.J., Plawsky, J.L., Wayner Jr., P.C., 2003. Experimental investigation of contact angle, curvature, and contact line motion in dropwise condensation and evaporation. J. Colloid Interf. Sci. 259, 354–366.

Hu, J., Chao, C., 2007. An experimental study of the fluid flow and heat transfer characteristics in micro-condensers with slug-bubbly flow. Int. J. Refrig. 30, 1309–1318.

Jaster, H., Kosky, P.G., 1976. Condensation in a mixed flow regime. Int. J. Heat Mass Transfer 19, 95–99.

Mederic, B., Miscevic, M., Miscevic, M., 2005. Void fraction invariance properties of condensation flow inside a capillary glass tube. Int. J. Multiphase Flow 31, 1049–1058.

Quan, X., Cheng, P., Wu, H., 2008. Transition from annular flow to plug/slug flow in condensation of steam in microchannels. Int. J. Heat Mass Transfer 51, 707–716.

Wang, H., Rose, J., 2005. A theory of film condensation in horizontal noncircular section microchannels. ASME J. Heat Transfer 125, 1096–1105.

Wu, H., Cheng, P., 2005. Condensation flow patterns in silicon microchannel. Int. J. Heat Mass Transfer 48, 2186–2197.

Wu, H., Yu, M., Cheng, P., Wu, X., 2007. Injection flow during steam condensation in silicon microchannels. J. Micromech. Microeng. 17, 1618–1627.

Wu, J., Chen, Y., Shi, M., Fu, P., Peterson, G., 2009. Three-dimensional numerical simulation for annual condensation in rectangular microchannels. Nanoscale Microscale Thermophys. Eng. 13, 13–29.

Zhang, Y.W., Faghri, A., 2001. Numerical simulation of condensation on a capillary grooved structure. Numer. Heat Transfer, Part A-Appl. 39, 227–243.

Zhang, Y.W., Faghri, A., Shafii, M.B., 2001. Capillary blocking in forced convective condensation in horizontal miniature channels. J. Heat Transfer 123, 501–511.

Zhang, W., Xu, J., Thome, J., 2008. Periodic bubble emission and appearance of an ordered bubble sequence (train) during condensation in a single microchannel. Int. J. Heat Mass Transfer 51, 3420–3433.

Zhao, T., Liao, Q., 2002. Theoretical analysis of film condensation heat transfer inside vertical mini triangular channels. Int. J. Heat Mass Transfer 45, 2829–2842.